UNIVERSITÀ DI PARMA
ARCHIVIO DELLA RICERCA

University of Parma Research Repository

Pulsed laser texturing for improved adhesive-bonded polyethylene (PE) joints

This is the peer reviewd version of the followng article:

note finali coverpage

(Article begins on next page)

22 December 2024

Pulsed laser texturing for improved adhesive-bonded polyethylene (PE) joints

Adrian H.A. Lutey*, Fabrizio Moroni

Dipartimento di Architettura e Ingegneria, Università di Parma, Parco Area delle Scienze 181/A, 43124 Parma, Italy

*Corresponding author: Tel: +39 0521 906029, Fax: +39 0521 905924, email: adrian.lutey@unipr.it

Nanosecond pulsed laser texturing was performed on pigmented polyethylene (PE) specimens with a 1064 nm fiber laser with the aim of improving adhesive-bonded joint strength. A Design-of-Experiments (DoE) was employed to optimize process parameters and determine the effects of average laser power, scanning velocity and hatch spacing on the resulting failure load of PE joints bonded with Teroson 9399. Failure load increased with laser energy dose up to the onset of macroscopic melting. Laser scanning strategies minimizing heat accumulation yielded best results as the energy dose could be increased as much as possible prior to onset of melting. The process exhibited highest sensitivity to heat accumulation in the laser scanning direction, favoring large pulse separation distances in the scanning direction and moderate pulse overlap in the lateral direction. With a focused spot diameter of 60 μm and a repetition rate of 20 kHz, a maximum failure load of 0.93 kN (1.49 MPa, standard deviation 0.01 kN) was achieved with a crossing-line laser scanning strategy, 25 μm hatch spacing, 3 W average power and 2500 mm/s scanning velocity. Under these conditions, purely cohesive failure took place yielding a 79 % improvement in failure load over standard primed joints.

Keywords: Laser Ablation; Nanosecond Pulses; Adhesives; Surface Preparation; Polymer; Polyethylene

1 INTRODUCTION

Engineering polymers find widespread use in industry due to their high performance-to-weight ratio and low cost compared to metal alloys. Friedrich [1] notes that plastics and carbon fiber reinforced plastics (CFRP) make up approximately 50% of materials used in next-generation low consumption concept vehicles. Polyethylene (PE) is a thermoplastic polymer that is widely employed due to its good chemical resistance, low friction coefficient, good impact strength and low cost. Applications include medical and healthcare devices, pipes and sliding guides for conveyor systems. The joining of plastic components is commonly performed with mechanical fasteners such as rivets and bolts. However, as discussed by Liu et al. [2], these techniques involve drilling, which increases manufacturing costs and reduces intrinsic joint strength. Moreover, mechanical fasteners do not provide sealed joints. Adhesive bonding can be effectively used to replace traditional joining systems due to its good strength, lower manufacturing cost and the possibility of connecting dissimilar materials. Polymer surfaces generally have a much lower surface energy than metals and inorganic compounds, making surface treatment essential for adhesive bonding (see Ebnesajjad [3]). The international standard ASTM D2093 [4] gives some guidelines for the preparation of plastic surfaces prior to adhesive bonding of test specimens, recommending mechanical preparation via abrasion or chemical treatment with a sulfuric acid-dichromate solution. The latter is highly toxic, presenting significant risks in terms of health and safety for which alternative technologies are preferred. More complex pre-treatment techniques have also been developed over recent years to allow the production of reliable polymeric bonded joints. Due to the diverse nature of polymers, however, each material requires definition of a specific treatment. For polyethylene (PE), in particular, Ebnesajjad [3] suggests chemical, oxidizing flame or plasma treatments, with the former consisting of immersion in a chromic acid solution.

An alternative to these approaches is the use of pulsed laser irradiation to induce precise material modification via thermal and non-thermal mechanisms, simplifying the pre-treatment process and eliminating the need for complex procedures and handling of chemicals. This technique has seen widespread application in improving the performance of composite and metallic adhesive-bonded joints. Galantucci and Gravina [5] employed a 25 ns pulsed excimer laser with emission wavelength of 248 nm to texture composite and metallic samples prior to adhesive bonding, demonstrating that laser irradiation led to increases in both surface wettability and roughness, ultimately increasing the maximum failure load by up to 96% for CFRP joints and 70% for aluminum joints compared to substrates subject to mechanical abrasion. Baburaj et al. [6] produced micro-column arrays on titanium surfaces with a nanosecond pulsed laser, achieving large increases in adhesive-bonded joint strength. They attributed these outcomes to increases in contact surface area, improved mechanical interlocking and increased wettability. Rechner et al. [7] instead employed a pulsed Nd:YAG laser with emission wavelength of 1064 nm for pre-treatment of aluminum alloy adhesive-bonded joints, achieving improvements in maximum failure load compared to reference samples both after bonding and after ageing in a salt spray environment. More recently, laser irradiation was successfully applied to metal surfaces by Loutas et al. [8], who showed that laser pre-treatment of aluminum specimens greatly improved both surface wettability and the average pealing load of adhesive-bonded joints compared to abraded and cleaned surfaces. Pan et al. [9] also demonstrated that laser ablation can effectively be applied to improving the interlaminar strength of CFRP/Mg laminates.

1

Laser technology plays an important role in industries where high quality and throughput are required. The nature of laser interaction with polymers is strongly dependent on the wavelength of the laser beam and optical properties of the material. Historically, laser processing of industrially relevant plastics such as PE, polypropylene (PP), polycarbonate (PC), polymethyl methacrylate (PMMA) and polyimide (PI) has mostly been performed with CO_2 lasers emitting at 10.6 µm or ultraviolet lasers emitting at <400 nm. In an early work investigating laser processing of plastics, Atanasov [10] successfully welded cylindrical PP and PC parts with a CO_2 laser, while Choudhury and Shirley [11] used the same type of laser source to cut PC, PP and PMMA, investigating the effects of processing parameters on the resulting outcomes. Coelho et al. [12] explored high-speed cutting of PE and PP films of thickness 10-100 µm with a CO_2 laser, achieving cutting speeds of up to 20 m/s. Dyer [13] instead provides a review of excimer laser processing of plastics in the UV, providing insight into the high resolution that can be achieved with this approach. As discussed by Caiazzo et al. [14] and Eltawahni et al. [15], laser irradiation at 10.6 µm leads to heating and melting, with material removal achieved via either vaporization and thermal degradation or through the use of assist gas to remove the molten phase. In an extensive review of photon-polymer interactions, Lippert [16] states that at wavelengths <400 nm, photothermal and photochemical effects combine to achieve material removal via both thermal and non-thermal pathways. In their pure forms, industrial plastics are largely transparent over the wavelength range 900 – 1100 nm, typical of modern CW and pulsed diode, fiber and disc laser sources employed for a wide range of metal processing applications such cutting, welding, marking and ablation. Ilie et al. [17] state that the efficiency of laser welding strongly depends on the optical properties of the polymers in question. As a result, the addition of specific additives to improve laser absorption is commonplace for processes such as transmission laser welding. Sohn et al. [18] instead show that non-linear absorption can be achieved with femtosecond laser pulses; however, equipment costs associated with this type of exposure may be prohibitive.

The situation is largely different for opaque pigmented polymers, where material response to CW or short-pulse (>1 ns) laser irradiation within the wavelength range 900 – 1100 nm is strongly dependent on the pigment employed and its concentration. The exact composition of industrial pigmented polymers is often difficult for manufacturers to acquire, for which sample analysis with an optical spectrometer is required or an appropriate experimental methodology must be developed to optimize laser parameters. In all cases, the low thermal conductivity and low melting and vaporization or degradation temperatures of plastics compared to metals leads to relatively high sensitivity to heat accumulation and development of a heat affected zone (HAZ). Where laser texturing is to be performed, macroscopic melting or degradation effects can erase the surface texture and strongly affect process outcomes. Nanosecond pulsed laser irradiation with limited pulse fluence and high laser scanning speeds are therefore preferable to obtain highly localized material response and limited heat accumulation. This has been confirmed by Lawrence and Li [19], who analyzed the effects of irradiation with four different laser types on the wettability and chemical composition of PE surfaces. Riveiro et al. [20], in analyzing the Raman spectra of untreated and laser-textured Ultra High Molecular Weight PE, noted that the material undergoes minor modification of its polymeric structure after laser irradiation. The main differences between the treated and untreated material were related to an increase in the amorphous character of the surfaces, suggesting melting of the surfaces followed by rapid cooling. The widespread use of Q-switched 1064 nm nanosecond pulsed fiber laser sources for industrial laser marking, together with difficulties in achieving strong and flexible adhesive-bonded polymer joints, suggest that insight into improving joint strength via pulsed laser texturing is of high value. Though Moroni et al. [21], Romoli et al. [22] and Sun et al. [23] recently implemented laser ablation with the aim of increasing the adhesion strength of metal and composite bonded joints, respectively, few works have dealt with this topic in relation to polymers, to the authors' knowledge, despite the potential that laser technology possesses in this application.

To address this issue, the present work sees an extensive experimental campaign based on a Design-of-Experiments (DoE) approach for optimizing nanosecond pulsed laser texturing of pigmented PE specimens for improved adhesive-bonded joint strength. Two different laser scanning strategies are tested, the first based on parallel-line exposures performed orthogonal to the direction in which force is to be applied, and the second based on crossed lines performed both orthogonal and parallel to the force direction. For each scanning strategy, two sets of experiments are performed to identify and optimize process parameters in terms of average laser power, scanning velocity and hatch spacing. It is shown that the joint failure load can be increased by 79 % compared to primed PE samples and one order of magnitude compared to washed samples, ultimately exceeding the shear strength of the adhesive itself.

2 MATERIALS AND METHODS

2.1 Samples and adhesive

Test samples were black pigmented PE (Tecafine PE 3) supplied by Ensinger Italia s.r.l (Milan, Italy) with dimensions 100 (l) × 25 (w) × 4 (h) mm. The adhesive employed for all tests was Teroson 9399, supplied by Henkel (Milan, Italy). The adhesive is a two-component, room-temperature curing system based on silane-modified polymers. Silane-modified adhesives combine good flexibility (elongation at failure typically greater than 100%) and good strength (typically in the range 1 – 10 MPa); therefore, they are suitable for producing flexible structural joints where the adhesive layer must withstand significant deformation. In particular, the selected adhesive represents a good choice for structural applications where materials with different thermal expansion coefficients must be connected. Good UV and weather resistance also make it suitable for external use. The main mechanical properties of the cured adhesive are summarized in Table 1. Currently, chemical adhesion promoters are recommended by the supplier for bonding of plastic surfaces.

2.2 Laser setup

Laser texturing of the PE samples was performed with a 1064 nm wavelength nanosecond pulsed ytterbium fiber laser source. Beam delivery was achieved via an optical fiber and collimator connected to a galvanometric scanning head for beam movement and an f-theta focusing lens with focal length of 160 nm, achieving a focused spot size of 60 µm. Samples were positioned on a micrometric vertical stage, with all tests performed with the target surface in the focal plane of the f-theta focusing lens. An exhaust system was employed with the intake adjacent to the sample during laser exposure to avoid optical absorption by the ablation products and accumulation of PE degradation products within the working area. The main characteristics and operating range of the laser setup are summarized in Table 2. Though the laser could emit an average power of up to 17 W, the maximum laser power utilized for experiments was 4 W due to strong interaction between the focused laser beam and pigmented polymer. A Gentec Maestro power meter was utilized to verify stable operation of the laser source and calibrate output down to 1 W average power.

Table 1 Main mechanical properties of Teroson 9399 [24].

Property	Value
Density	1.35 g/cm³
Tensile Strength	approx. 3.0 MPa
Elongation at Break	approx. 150%
Tensile Shear Strength	approx. 2.0 MPa
Shore-A Hardness	approx. 55 MPa

Table 2 Main characteristics and operating range of laser setup

Parameter	Value
Make	LaserPoint
Model	YFL 20P
Emission wavelength	1064 nm
Pulse duration	104 ns
Repetition rate	20 kHz
Average laser power (P)	1 – 17 W
Pulse energy (E_p)	50 – 850 µJ
Beam quality (M^2)	1.8
Focused Gaussian spot diameter (d_0)	60 µm
Rayleigh range	1.45 mm
Peak pulse fluence (F_p)	3.5 – 60.1 J/cm^2
Maximum beam scanning velocity (v)	2.5 m/s

2.3 Laser texturing

Laser irradiation was performed over areas of 25 × 25 mm on the PE specimens while varying the average laser power, P, scanning velocity, v, and lateral hatch spacing, h. For each repetition and parameter set, two identical specimens were textured to allow preparation of an adhesive-bonded joint between the treated surfaces. Peak pulse fluence, F_p, was calculated in its standard form for a Gaussian intensity distribution:

$$F_p = \frac{8E_p}{\pi d_0^2} \tag{1}$$

where E_p is the pulse energy and d_0 is the focused Gaussian spot diameter. Scanning velocity, together with the repetition rate, dictated the longitudinal pulse separation distance and therefore distance between single-pulse ablation features. The hatch spacing was instead equal to the lateral pulse separation distance. These process parameters all influenced the energy dose and therefore macroscopic heat accumulation and melting effects. The average energy dose, E, was calculated as:

$$E = \frac{P}{vh} \tag{2}$$

Two laser scanning strategies were employed for experiments. The first comprised parallel lines (PL) orthogonal to the direction in which force was applied during tensile tests; the second comprised crossed lines (CL) both orthogonal and parallel to the force direction. Preliminary tests were first performed to establish the macroscopic parameter range over which an appropriate level of laser interaction could be achieved without excessive melting or burning. Complete melting of the irradiated surface was observed with an average laser power of 2 W, scanning velocity of 100 mm/s and hatch spacing of 50 μm, providing an approximate upper limit of 40 J/cm^2 for the applied laser energy dose. Subsequent tests were performed with an average laser power of 2 W, hatch spacing of 100 μm and scanning velocity over the range 100-1500 mm/s for the PL and 200-2500 mm/s for the CL scanning strategies. The resulting surfaces exhibited topographies ranging from incisions approximately 50 μm in depth at low scanning velocity to a series of small protrusions at high scanning velocity. Adhesive joints produced with these parameters exhibited low strength where deep incisions were present. Over the preliminary parameter range, maximum joint strength was achieved with a scanning velocity of 1250 mm/s for PL and 1500 mm/s for CL scanning strategies. A central parameter set with an average laser power of 2 W, hatch spacing of 100 μm and scanning velocity of 1400 mm/s was therefore chosen for the tests described below.

A Design-of-Experiments (DoE) was then developed for systematic variation of process parameters with both PL and CL laser scanning strategies. As extensively addressed by Montgomery and Runger [25], the aim of a DoE is to provide a systematic framework for planning experiments to robustly describe variations in the response of a system as a result of specific changes made to input variables so as to identify the potential causes of the observed response. This approach was employed with the aim of determining the dependence of adhesive-bonded joint strength on the average laser power, scanning velocity and hatch spacing used for laser treatment. These characteristic input variables where chosen due to their direct influence on the physical nature of laser-material interaction. At constant laser repetition rate and focused spot size (20 kHz and 60 μm, respectively, Table 2), the average power dictated the laser pulse fluence and therefore the nature of interaction between the focused laser beam and target material during a single laser pulse. The scanning velocity and hatch spacing instead dictated the pulse overlap in the longitudinal and lateral directions, respectively, and therefore coverage of the target surface area.

A first set of experiments was performed based on a randomized two-level factorial DoE with three factors: average power, scanning velocity and hatch spacing. This type of DoE allows the individual and combined effects of all factors on the response to be determined. The specific design involved three repetitions of all external points in Fig. 1(a) and five repetitions of the central point. This configuration was chosen to highlight the macroscopic effects of process parameters and assess repeatability. Values corresponding to the levels of each factor are specified in Table 3, together with the overall range of the tested pulse fluence (Eq. (1)), pulse spacing and average energy dose (Eq. (2)). It must be noted that the three factors were varied independently over the respective levels given in Table 3. All tested combinations of process parameters can also be found in Tables 10 and 11 in the Appendix for the PL and CL scanning strategies, respectively. Analysis of variance (ANOVA), discussed extensively by Montgomery and Runger [25], was performed on the outcomes for each scanning strategy to attribute variations in system output to their source, assess model adequacy, and consequently define parameter ranges over which optimized experiments could be performed.

4

For optimization, different parameter ranges were employed for PL and CL scanning strategies based on the outcomes of the first set of experiments. These tests were performed based on a randomized central composite DoE with an axial spacing of 1 due to limitations in the maximum scanning velocity of the focused laser beam. This involved two repetitions of all external points in Fig. 1(b) and four repetitions of the central point. This configuration was chosen to efficiently model process outcomes with as few tests as possible. Values corresponding to the levels of each factor are specified in Table 4 for the PL scanning strategy and Table 5 for the CL scanning strategy, together with the overall range of tested pulse fluence, pulse spacing and average energy dose. All tested combinations of process parameters can also be found in Tables 12 and 13 in the Appendix for the PL and CL scanning strategies, respectively. The optimized parameter sets generally involved similar average laser energy doses to the first group of tests, but higher longitudinal pulse spacing and lower lateral pulse spacing. As will be discussed later, this was due to detrimental heat accumulation effects taking place preferentially in the laser scanning direction. Analysis of variance (ANOVA) was again performed on the outcomes for each scanning strategy. Statistical analyses were performed with the commercial software Design Expert 7.0 (StatEase, Minneapolis USA) [26].

Table 3 Two-level factorial DoE levels and resulting parameter ranges for first set of experiments. Specific combinations of parameter levels used for individual tests are presented in Fig. 1(a). Both PL and CL scanning strategies employed the same experimental parameters.

Parameter	Level #1	Centre	Level #2
Average power (P)	1 W	2 W	3 W
Scanning velocity (v)	700 mm/s	1400 mm/s	2100 mm/s
Hatch spacing (h)	50 µm	100 µm	150 µm
Peak pulse fluence (F_p)	$3.5 - 10.6$ J/cm^2		
Long. pulse spacing	$35 - 105$ µm		
Lat. pulse spacing	$50 - 150$ µm		
Av. energy dose (E)	$0.32 - 8.6$ J/cm^2		

Table 4 Central composite DoE levels and resulting parameter ranges for optimization of PL scanning strategy. Specific combinations of parameter levels used for individual tests are presented in Fig. 1(b).

Parameter	Level #1	Centre	Level #2
Average power (P)	2 W	3 W	4 W
Scanning velocity (v)	1700 mm/s	2100 mm/s	2500 mm/s
Hatch spacing (h)	25 µm	37.5 µm	50 µm
Peak pulse fluence (F_p)	$7.1 - 14.2$ J/cm^2		
Long. pulse spacing	$85 - 125$ µm		
Lat. pulse spacing	$25 - 50$ µm		
Energy dose (E)	$1.6 - 9.4$ J/cm^2		

Table 5 Central composite DoE levels and resulting parameter ranges for optimization of CL scanning strategy. Specific combinations of parameter levels used for individual tests are presented in Fig. 1(b).

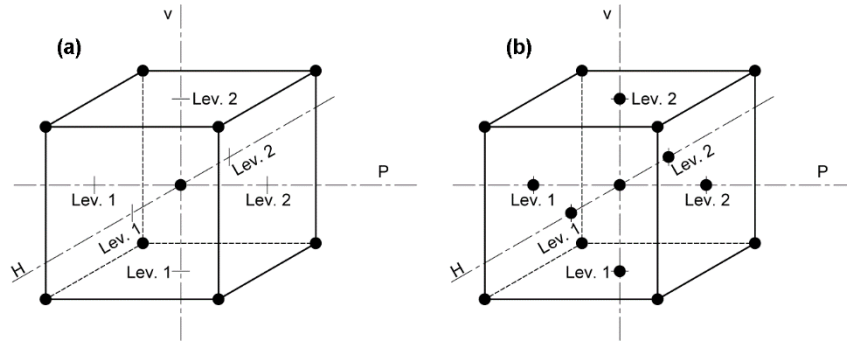| Parameter	Level #1	Centre	Level #2
Average power (P)	1 W	2 W	3 W
Scanning velocity (v)	1700 mm/s	2100 mm/s	2500 mm/s
Hatch spacing (h)	25 µm	37.5 µm	50 µm
Peak pulse fluence (F_p)	$3.5 - 10.6$ J/cm^2		
Long. pulse spacing.	$85 - 125$ µm		
Lat. pulse spacing	$25 - 50$ µm		
Energy dose (E)	$1.6 - 14.1$ J/cm^2		

Fig. 1 (a) Two-level factorial DoE for first set of experiments. Each point represents a combination of tested parameter levels specified within Table 3; (b) Central composite DoE for second set of experiments. Each point represents a combination of the tested parameter levels specified within Table 4 for the PL scanning strategy and Table 5 for the CL scanning strategy.

2.4 Surface characterization

All laser-textured PE samples were characterized with a Taylor Hobson TalySurf green light coherence correlation interferometry (CCI) non-contact automated optical profiler prior to bonding of the adhesive joints. The instrument exploits division of amplitude interference to determine small differences in surface topography. The instrument was equipped with a 50× objective with numerical aperture of 0.55 in a Mirau interferometer configuration with a 1 MP camera, providing a resolution of <1nm in the vertical direction up to a maximum slope of 27.5° and a resolution of 0.4 µm in the horizontal plane over a 346 × 346 µm sampling area. A piezoless automated z-axis scanner provided vertical movement of the objective during acquisition of the surface profile, while an automated x-y stage with manual tip-tilt function allowed movement of the sample in the horizontal plane and rotation about the x and y axes. Numerical data stitching from four acquisitions was performed to obtain topography maps over an area of 610 × 610 µm for each set of laser parameters. Data processing was performed with the Taylor Hobson TalyMap software. Data obtained with the optical profiler was employed to visualize and verify the resulting surface topography, as well as quantify the average areal surface roughness, S_a, in line with ISO 25178-2 [27], with which the resulting joint failure load was correlated.

2.5 Adhesive joint production

Two PE plates were bonded to produce the joint geometry shown in Fig. 2. The adhesive thickness, t, and the overlap length, OL, were set to 1.2 mm and 25 mm, respectively.
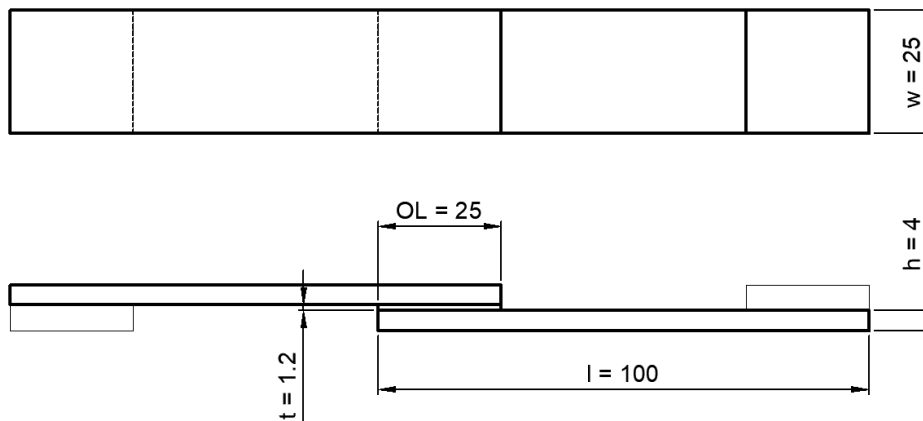

Fig. 2 Geometry and dimensions of the tested joints

The PE specimens were initially wiped with a clean cloth to remove dust and other impurities from the surface. The substrates were then laser textured in line with the procedure described in Section 2.3 and assembled with the adhesive within one hour. The overlap and adhesive thickness were controlled with an appropriate jig. Joints were tested after being stored in ambient conditions for one week to ensure complete curing of the adhesive had taken place.

In order to provide reference values for failure load, additional samples were produced with the same bonding method but with the following preparation methods: i) washed joints, where the surfaces were simply washed with soap and water, and ii) primed joints, where the surfaces were brushed with Teroson PP33, a specific

6

primer for polymeric substrates. In all cases, samples were dried in ambient air for 30 minutes prior to preparation of the adhesive-bonded joints. Three samples were produced for each set of reference joints.

2.6 Tensile test setup and procedure

Tensile shear tests were performed based on the international standard ASTM D3163 [28]. The specimens were tested with an INSTRON 4400 tensile testing machine equipped with a 30 kN load cell. Alignment tabs, represented by the light gray rectangles in Fig. 2, were bonded with the same adhesive (i.e. Teroson 9399) at the end of each substrate to avoid the introduction of artificial bending when the specimens were clamped and loaded in the testing machine. Tests were carried out under displacement control at a speed of 3 mm/min. This speed was chosen to achieve joint failure in approximately three minutes and avoid secondary effects such as creep and visco-elasticity due to excessively low strain rates or brittle behavior due to excessively high strain rates. Load versus displacement curves were recorded for each specimen, and the failure load was identified as the maximum load registered during test. An example load-displacement curve is shown in Fig. 3, corresponding to a single test specimen prepared with a PL scanning strategy, hatch spacing of 37.5 µm, average laser power of 4 W and scanning velocity of 2100 mm/s.
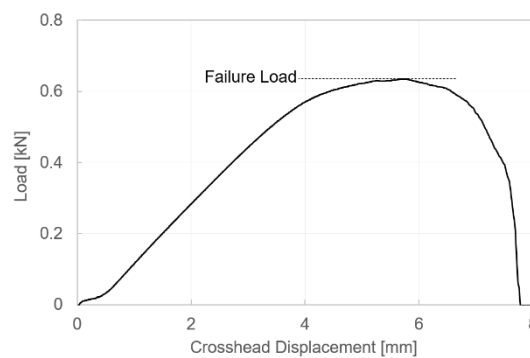

Fig. 3 Example of experimental load versus displacement curve

3 RESULTS AND DISCUSSION

3.1 Washed and primed samples

The three washed specimens achieved an average failure load of 0.075 kN (0.12 MPa) and a standard deviation of 0.0015 kN, while the three primed joints achieved an average failure load of 0.52 kN (0.83 MPa) and a standard deviation of 0.048 kN. These outcomes were considered poor due to interfacial failure between the adhesive and substrate, resulting in joint strength well below the adhesive shear strength declared by the supplier (approx. 2 MPa). Primed samples nonetheless provided somewhat higher strength than washed samples.

3.2 Energy dose and average areal roughness

Prior to detailed analysis of the effects of laser interaction, the general influence of laser energy dose and average areal surface roughness on the resulting failure load of the adhesive-bonded PE joints was considered for all tested parameters groups. Data presented in Fig. 4 show that the failure load generally increases with both laser energy dose and average areal surface roughness from minimum values for untreated samples to maximum values in the range 2.5 – 10 J/cm^2 for energy dose and 1.5 – 3.5 µm for average areal surface roughness. Joint failure load remains relatively stable with further increases in both parameters prior to a decrease in failure load for high values of energy dose and roughness. The resulting surface texture from laser irradiation generally increases mechanical interlocking up to a maximum, after which additional laser interaction is no longer beneficial or becomes detrimental. Given the thermal nature of nanosecond pulsed laser interaction with pigmented PE, excessive energy dose within any one parameter group may have increased the risk of melting and degradation of the polymer surface due to heat accumulation, which may have resulted in the lower observed joint strength. With very high surface roughness, issues relating to lack of adhesive flow into deep craters and channels may also have influenced the results, as has been observed in previous studies [21,22]. While these trends can be observed for all parameter groups, there are notable differences between optimum values for each group of experiments, as well as variations within each group. The physical reasons for these differences will be examined in detail in the following paragraphs.
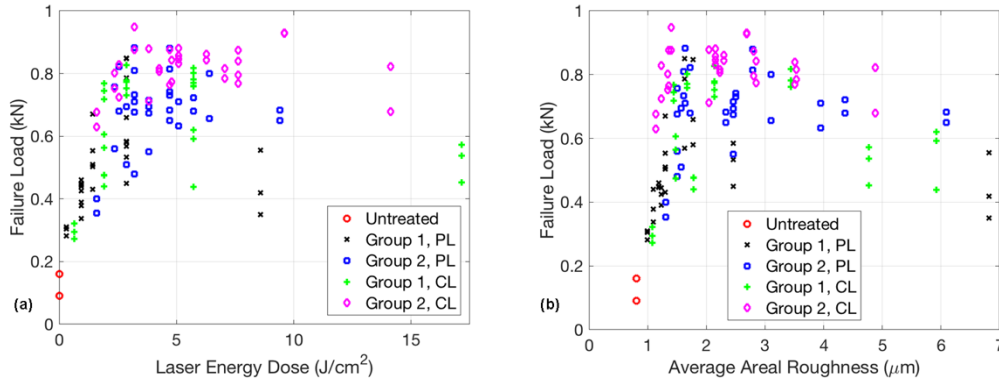
Fig. 4 Maximum experimental joint failure load as functions of: (a) average laser energy dose and (b) average areal roughness

3.3 PL scanning strategy, test group 1

The outcomes of ANOVA performed on the first group of experiments with the PL scanning strategy are presented in Fig. 5, together with experimental data from each test. The corresponding model equation for the failure load is:

$$L = 1.53 - 0.45P - 6.8 \times 10^{-3}h - 5.8 \times 10^{-4}v + 3.2 \times 10^{-3}Ph + 3.0 \times 10^{-4}Pv + 3.1 \times 10^{-6}hv - 2.0 \times 10^{-6}Phv \qquad (3)$$

Where L is the failure load (kN), P the average laser power (W), h the hatch spacing (µm) and v the scanning velocity (mm/s). The model F-value was 8.93, significant, while the lack of fit F-value was 0.9, insignificant. A full summary of ANOVA outcomes can be found in Table 6 in the Appendix, while the average failure load and standard deviation of each parameter set can be found in Table 10. An increase in failure load is generally achieved at lower hatch spacing, while optimum laser power varies with scanning velocity. Highest average joint failure load is achieved with 50 µm hatch spacing, 1 W average laser power and 700 mm/s scanning velocity (point *A* in Fig. 5), corresponding to an average energy dose of 2.9 J/cm². This result is closely followed by the same hatch spacing, 3 W average laser power and 2100 mm/s scanning velocity (point *B* in Fig. 5), corresponding to the same energy dose. Upon further analysis, it can be observed that 150 µm hatch spacing, 3 W laser power and 700 mm/s velocity (point *C* in Fig. 5) also corresponds to the same average energy dose but achieves lower joint strength. This outcome can be accounted for in terms of heat accumulation, which takes place preferentially in the laser scanning direction. Heat accumulation is instead less severe in the lateral (hatch) direction as the period between successive adjacent laser pulses is orders of magnitude higher than in the longitudinal direction, allowing more time for thermal conduction into the bulk material. With the same average energy dose but lower hatch spacing, thermal deposition and peak temperatures with each laser pass are therefore lower. Due to the relatively low melting and thermal degradation temperatures of PE, minimization of the peak temperature resulting from heat accumulation is critical to ensuring the resulting surface topography from laser ablation is not eliminated by macroscopic melting effects. With deviation from one of the three conditions discussed above (points *A* to *C* in Fig. 5), joint failure load becomes lower due to either excessive laser interaction for energy doses higher than 2.9 J/cm² (higher laser power or lower scanning velocity) or insufficient laser interaction for lower doses (lower laser power or higher scanning velocity). In light of these results, and bearing in mind productivity requirements favoring faster laser scanning strategies, the parameter range selected for optimization of the PL strategy (Table 4) was chosen to span a similar energy dose range but with lower hatch spacing, higher average laser power and higher scanning velocity.
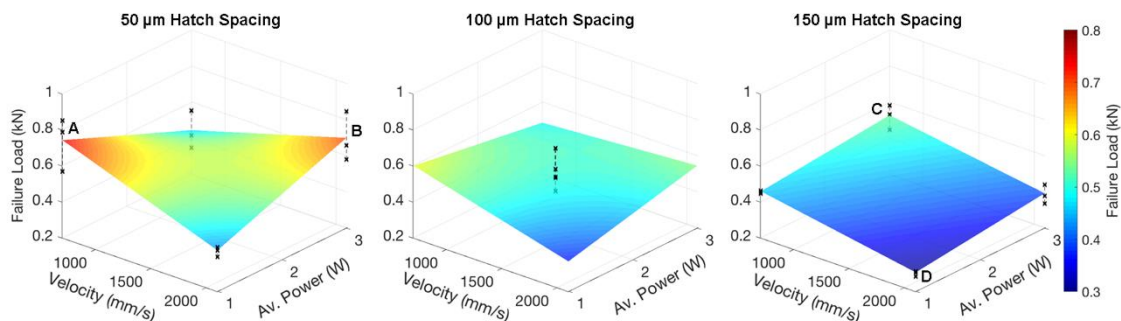

Fig. 5 ANOVA model results and experimental data for group 1, PL scanning strategy

The topography of selected laser-textured surfaces from the first group of tests with the PL scanning strategy are displayed in Fig. 6, together with the laser parameters and experimental fracture surfaces. The left-hand image corresponds to the surface achieving lowest average failure load (0.30 kN / 0.48 MPa, standard deviation 0.01 kN) with a hatch spacing of 150 μm, average laser power of 1 W and scanning velocity of 2100 mm/s (point *D* in Fig. 5). The topography is characterized by small protrusions separated by 105 μm in the longitudinal direction and 150 μm in the lateral direction, where limited laser interaction has led to partial ejection of melted material. These characteristics are sufficient to achieve modest improvements in shear strength compared to the washed samples; however, the fracture surface shows clear evidence of interfacial failure. The effects of laser interaction are instead more accentuated in the right-hand image, which corresponds to the surface achieving highest average failure load (0.69 kN / 1.10 MPa, standard deviation 0.14 kN) with a hatch spacing of 50 μm, average laser power of 3 W and scanning velocity of 2100 mm/s (point *B* in Fig. 5). In this case, the surface is characterized by a series of raised lines separated by 105 μm in the longitudinal direction. With hatch spacing (50 μm) marginally less than the focused laser spot diameter (60 μm), pulse overlap in this direction, together with stronger laser interaction due to higher pulse fluence, leads to a series of mostly uninterrupted ridges. The resulting fracture surface shows evidence of mixed interfacial-cohesive failure, with prevalence of the latter. As noted previously, larger pulse spacing in the laser scanning direction than in the hatch direction leads to reduced heat accumulation effects and therefore lower peak temperatures, which ultimate translate into lower risk of macroscopic melting and degradation of the surface topography.
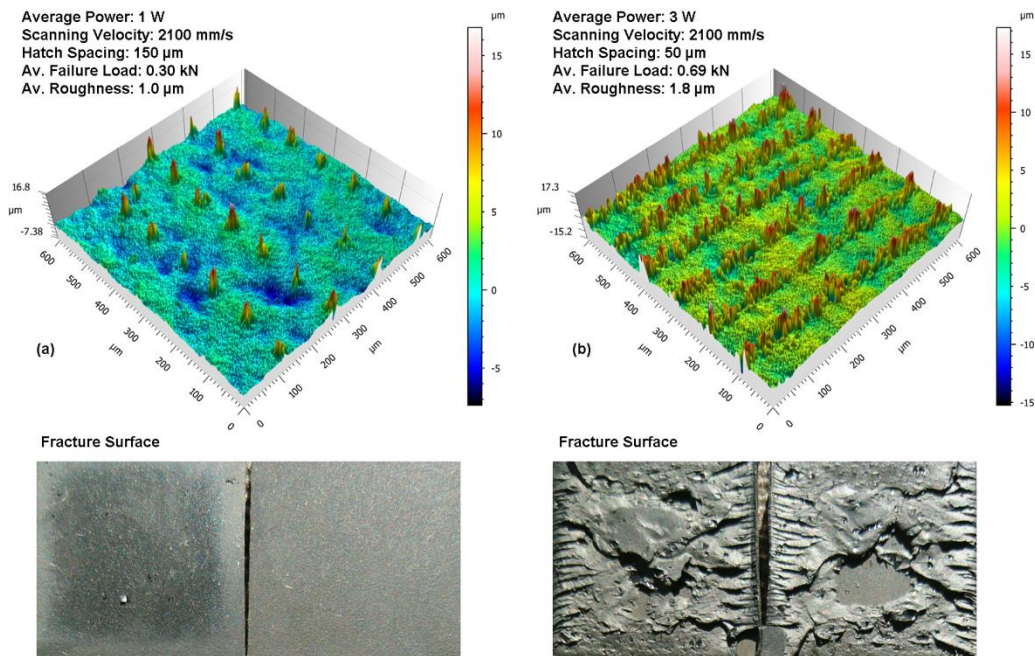

Fig. 6 Measured topography of selected laser-treated surfaces and photographs of corresponding fracture surfaces for group 1, PL scanning strategy. Photographs show both 25 × 25 mm facture surfaces for each individual test specimen.

3.4 PL scanning strategy, test group 2

Figure 7 displays the results of ANOVA for the second group of experiments performed with the PL scanning strategy, together with experimental data from each test. The corresponding model equation for the failure load is:

$$L = 1.30 - 0.35P + 1.9 \times 10^{-3}h + 9.8 \times 10^{-5}v + 5.3 \times 10^{-3}Ph + 7.3 \times 10^{-5}Pv - 1.1 \times 10^{-5}hv \qquad (4)$$

The model *F*-value was 5.87, significant, while the lack of fit *F*-value was 1.33, insignificant. A full summary of ANOVA outcomes can be found in Table 7 in the Appendix, while the average failure load and standard deviation of each parameter set can be found in Table 11. As with the previous case, higher joint failure load is achieved with lower hatch spacing, though differences across the tested parameter range are generally more limited. Lowest joint strength is achieved with 50 μm hatch spacing, 2 W average laser power and 2500 mm/s scanning velocity (point *B* in Fig. 7), corresponding to an average energy dose of 1.6 J/cm². Maximum joint failure load is instead achieved with a hatch spacing of 25 μm, average laser power of 2 W and scanning

velocity of 1700 mm/s (point *A* in Fig. 7), corresponding to an average energy dose of 4.7 J/cm^2. The results exhibit low sensitivity to scanning velocity at 2 W average laser power and low sensitivity to average laser power at 2500 mm/s scanning velocity, with average failure load consistently above 0.7 kN (1.12 MPa). These outcomes represent a stable, optimized process with relatively low sensitivity to small variations in input parameters.
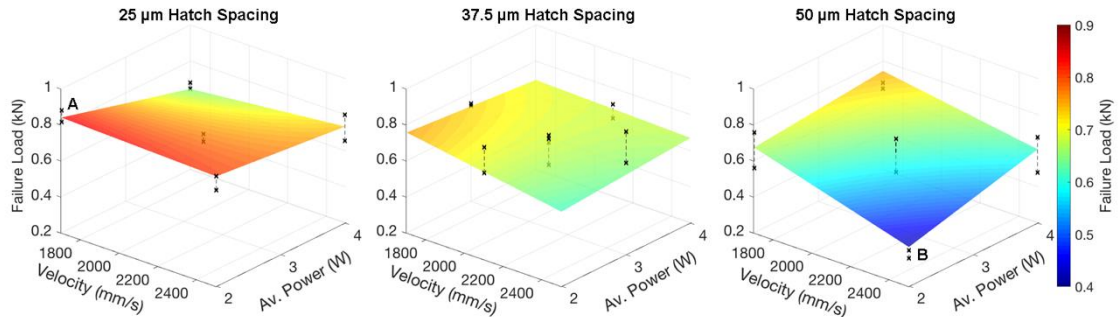

Fig. 7 ANOVA model results and experimental data for group 2, PL scanning strategy

The topography of surfaces corresponding to the highest and lowest joint strength from the same test group are shown in Fig. 8, together with the laser parameters and experimental fracture surfaces. The left-hand image corresponds to the surface achieving lowest failure load (0.38 kN / 0.61 MPa, standard deviation 0.02 kN) with a hatch spacing of 50 µm, average laser power of 2 W and scanning velocity of 2500 mm/s (point *B* in Fig. 7). The resulting surface topography is a series of small protrusions separated by 125 µm in the longitudinal direction and 50 µm in the lateral direction. Despite some overlap in the lateral direction, laser interaction is inadequate to produce continuous ridges, leading to lower joint strength and interfacial failure as observed in the previous case. The right-hand image instead corresponds to the surface achieving maximum failure load (0.85 kN / 1.36 MPa, standard deviation 0.03 kN) with a hatch spacing of 25 µm, average laser power of 2 W and scanning velocity of 1700 mm/s (point *B* in Fig. 7). In this case, the surface is quite similar to the best result obtained in the first group (Fig. 6(b)). The main difference in this case is better-defined geometry and slightly higher ridges with a hatch spacing of 25 µm due to the higher lateral pulse overlap. Ridge spacing is also lower, 85 µm, due to the lower scanning velocity; however, the experimental joint strength exhibits relative low sensitivity to changes in this parameter. The outcome is a condition in which the interface strength is greater than that of the adhesive itself and completely cohesive failure takes place, leading to consistently high joint strength with limited data dispersion.
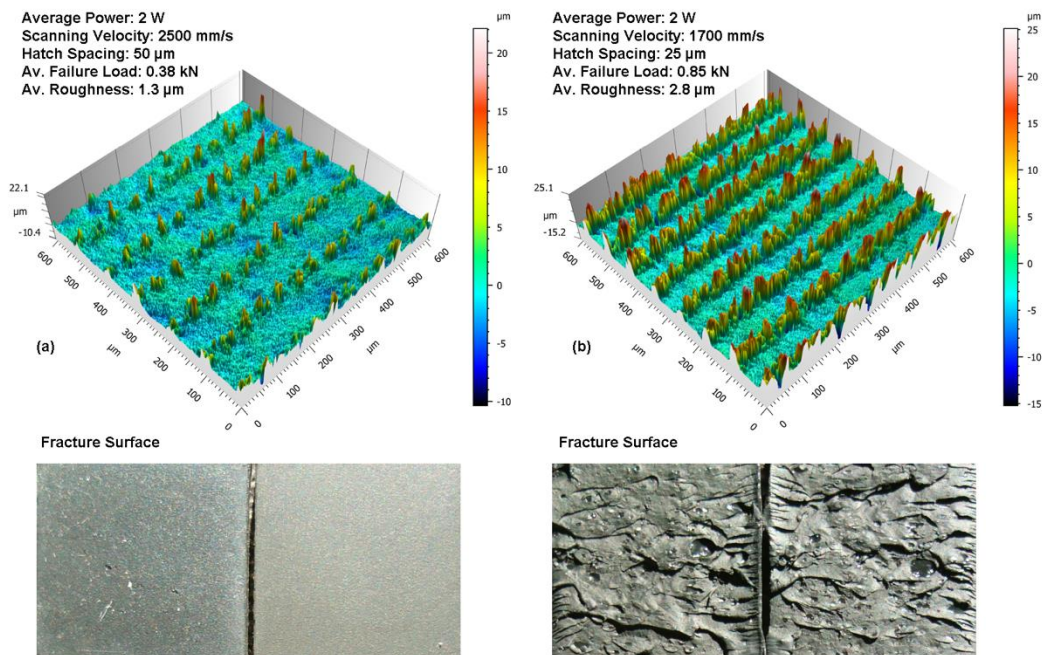

Fig. 8 Measured topography of selected laser-treated surfaces and photographs of corresponding fracture surfaces for group 2, PL scanning strategy. Photographs show both 25 × 25 mm facture surfaces for each individual test specimen.

3.5 CL scanning strategy, test group 1

The outcomes of ANOVA for the first group of experiments performed with the CL scanning strategy are presented in Fig. 9, together with experimental data from each test. The corresponding model equation for the failure load is:

$$L = 1.17 - 0.28P - 2.8 \times 10^{-3}h - 7.6 \times 10^{-5}v + 1.6 \times 10^{-3}Ph + 1.3 \times 10^{-4}Pv - 1.1 \times 10^{-6}hv - 4.8 \times 10^{-7}Phv \qquad (5)$$

The model F-value was 9.74, significant, while the lack of fit F-value was 61.6. The latter was considered unacceptable, signifying an inappropriate parameter range for the DoE. Attention was therefore paid to selecting a more appropriate parameter range for the second group of experiments based purely on the experimental results achieved in the first group. A full summary of ANOVA outcomes can be found in Table 8 in the Appendix, while the average failure load and standard deviation of each parameter set can be found in Table 12. As with the PL scanning strategy, lower hatch spacing generally leads to increases in failure load; however, the relationship between laser power and scanning velocity is more complex than in the previous cases. Joint failure load is relatively insensitive to variations in average laser power for 50 μm hatch spacing and 2100 mm/s scanning velocity, or for 150 μm hatch spacing and 700 mm/s scanning velocity. With 100 μm hatch spacing, experimental results attain intermediate values. These outcomes suggest a more robust process with lower sensitivity to variations in average laser energy dose, which is twice that of the PL scanning strategy for the same laser parameters due to the two orthogonal laser passes. The relatively long time delay between laser passes from different scanning directions allows more aggressive surface modification with higher total energy doses and lower sensitivity to this parameter, as can also be seen in Fig. 4(a). Highest average joint failure load is achieved with 50 μm hatch spacing, 3 W average laser power and 2100 mm/s scanning velocity (point *B* in Fig. 9), corresponding to an average energy dose of 5.7 J/cm^2. As with the PL scanning strategy, a similar result is achieved with the same hatch spacing, 1 W average laser power and 700 mm/s scanning velocity (point *A* in Fig. 9), while lower joint failure load is achieved with 150 μm hatch spacing, 3 W average laser power and 700 mm/s scanning velocity (point *C* in Fig. 9), both corresponding to the same average energy dose. The underlying reasons for these outcomes are the same as for the PL scanning strategy. Due to observed improvements with lower hatch spacing and higher scanning velocity (at 50 μm hatch spacing), together with relatively low sensitivity to laser power under these conditions, the parameter range selected for optimization of the CL strategy (Table 5) was chosen with lower hatch spacing, the same laser power and higher scanning velocity.
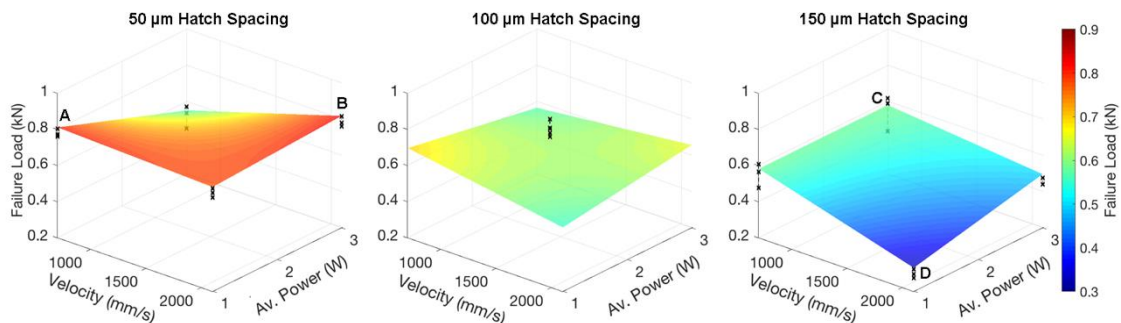

Fig. 9 ANOVA model results and experimental data for group 1, CL scanning strategy

The topography of selected surfaces from the same test group are shown in Fig 10, together with the laser parameters and experimental fracture surfaces. The left-hand image corresponds to the surface achieving lowest average failure load (0.3 kN / 0.48 MPa, standard deviation 0.02 kN) with a hatch spacing of 150 μm, average laser power of 1 W and scanning velocity of 2100 mm/s (point *D* in Fig. 9). These parameters are the same as in Fig. 6(a) but with a CL laser scanning strategy. As such, the surface is characterized by small protrusions obtained with the same laser pulse fluence as for the PL strategy but with a higher feature density due to the additional orthogonal laser pass. The distance between peaks is variable in this case due to the 105 μm longitudinal and 150 μm lateral pulse spacing for both laser passes in different directions. The average failure load obtained with these parameters is the same as for the corresponding PL samples, while the fracture surface shows clear evidence of interfacial failure, suggesting that overly large pulse separation distances and low laser pulse fluence are inappropriate for achieving effective mechanical interlocking with the adhesive. The effects of laser interaction are more clearly defined in the right-hand image, corresponding to the surface achieving highest average failure load (0.79 kN / 1.26 MPa, standard deviation 0.03 kN) with a hatch spacing of 50 μm, average laser power of 3 W and scanning velocity of 2100 mm/s (point *B* in Fig. 9). Again, these are

11

the same laser parameters as in Fig. 6(b) but with a CL scanning strategy. In this case, the topography is effectively a "checkerboard" of ridges separated by 105 µm in both directions, corresponding to the longitudinal pulse spacing obtained with a scanning velocity of 2100 mm/s and a pulse repetition rate of 20 kHz. The resulting fracture surface is predominately cohesive, with very limited evidence of interfacial failure. As with the CL scanning strategy, higher longitudinal pulse spacing and lower lateral pulse spacing is preferential due to a reduction in heat accumulation taking place in the laser scanning direction.
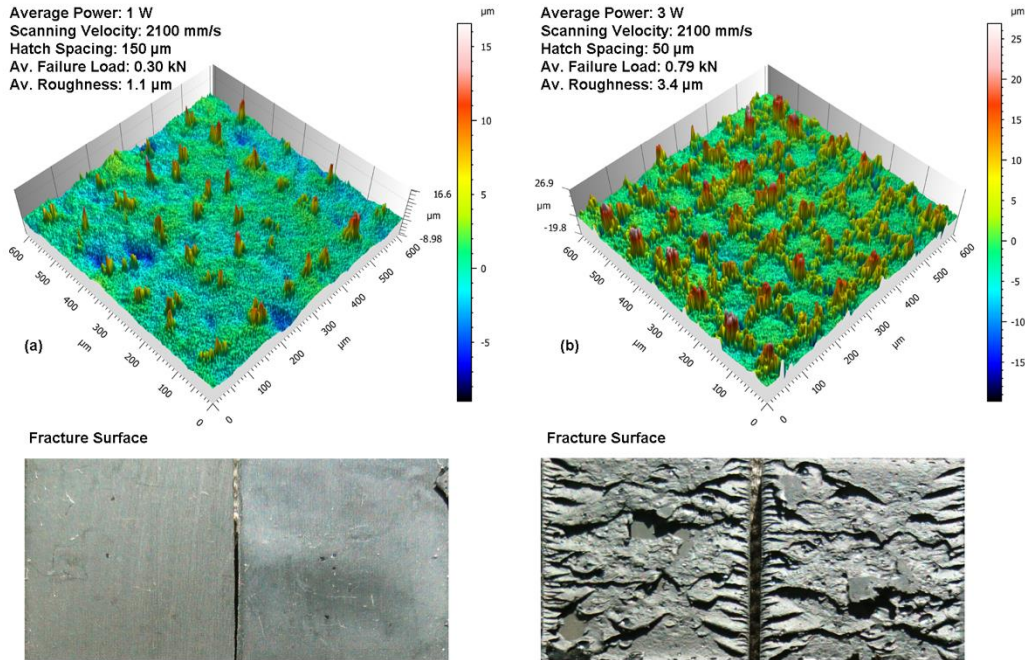

Fig. 10 Measured topography of selected laser-treated surfaces and photographs of corresponding fracture surfaces for group 1, CL scanning strategy. Photographs show both 25 × 25 mm facture surfaces for each individual test specimen.

3.6 CL scanning strategy, test group 2

The results of ANOVA and experimental data from the second group of experiments performed with the CL scanning strategy are shown in Fig. 11. The corresponding model equation for the failure load is:

$$L = 0.55 - 0.21P + 1.2 \times 10^{-2}h + 2.5 \times 10^{-4}v + 2.3 \times 10^{-3}Ph + 6.8 \times 10^{-5}Pv - 9.7 \times 10^{-6}hv \tag{6}$$

The model *F*-value was 6.24, significant, while the lack of fit *F*-value was 0.79, insignificant. A full summary of ANOVA outcomes can be found in Table 9 in the Appendix, while the average failure load and standard deviation of each parameter set can be found in Table 13. Higher joint strength is again achieved with lower hatch spacing, with relatively low sensitivity to average laser power and scanning velocity in most cases. Lowest joint failure load is achieved with a hatch spacing of 50 µm, average laser power of 1 W and scanning velocity of 2500 mm/s (point *B* in Fig. 11), corresponding an average energy dose of 1.6 J/cm^2. Maximum joint strength is instead achieved with a hatch spacing of 25 µm, average power of 3 W and scanning velocity of 2500 mm/s (point *A* in Fig. 11), corresponding to an energy dose of 9.6 J/cm^2. There is little variation in experimental outcomes under these conditions with a reduction in average laser power down to 1 W, corresponding to an average energy dose of 3.2 J/cm^2. Such a large parameter range in which good joint strength is achieved is due to the use of higher scanning velocities and two laser passes in orthogonal directions, allowing relatively aggressive surface modification while minimizing heat accumulation and macroscopic melting. Low average power and therefore energy dose is nonetheless sufficient for achieving high joint strength.
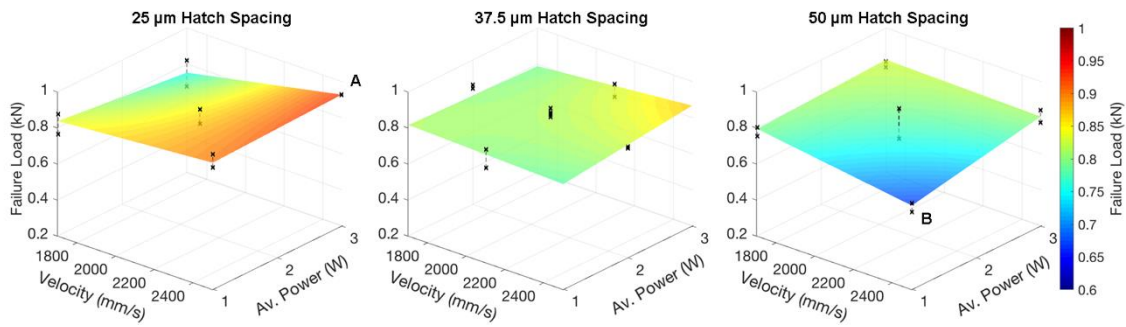
12

Fig. 11 ANOVA model results and experimental data for group 2, CL scanning strategy

The topography of surfaces corresponding to the highest and lowest failure loads from the same test group are presented in Fig. 12, together with the laser parameters and experimental fracture surfaces. The left-hand image, corresponding to an average failure load of 0.65 kN (1.04 MPa, standard deviation 0.03 kN) achieved with a hatch spacing of 50 µm, average laser power of 1 W and scanning velocity of 2500 mm/s (point *B* in Fig. 11), shows a partially-defined "checker-board" effect where marginal pulse overlap in the lateral direction has led to discontinuous ridges in both scanning directions. This effect is sufficient to achieve similar outcomes to the best results achieved with the PL scanning strategy in the first group; however, it is clear from the fracture surface that predominantly interfacial failure continues to take place. The right-hand image, corresponding to an average failure load of 0.93 kN (1.49 MPa, standard deviation 0.01 kN) achieved with 25 µm hatch spacing, 3 W average power and 2500 m/s scanning velocity (point *A* in Fig. 11), shows a well-defined "checker-board" effect where high pulse overlap in the lateral direction has instead led to continuous ridges in both scanning directions. In terms of surface topography, a higher surface feature density in the absence of macroscopic melting leads to higher joint strength up to the limit of adhesive failure. Though surface topography and therefore joint strength resulting from nanosecond pulse laser irradiation of PE are generally quite sensitivity to the selection of laser parameters, a high-velocity CL scanning strategy with average energy dose in the range 3.2 – 9.6 J/cm² leads to robust results with low variation in joint strength with changes in scanning velocity and average laser power. This outcome is due to homogeneous deposition of laser energy and high longitudinal pulse spacing, resulting in the least possible heat accumulation and melting. The resulting fracture surface is therefore purely cohesive and the average failure load the highest of all tests, approaching the nominal strength of the adhesive.
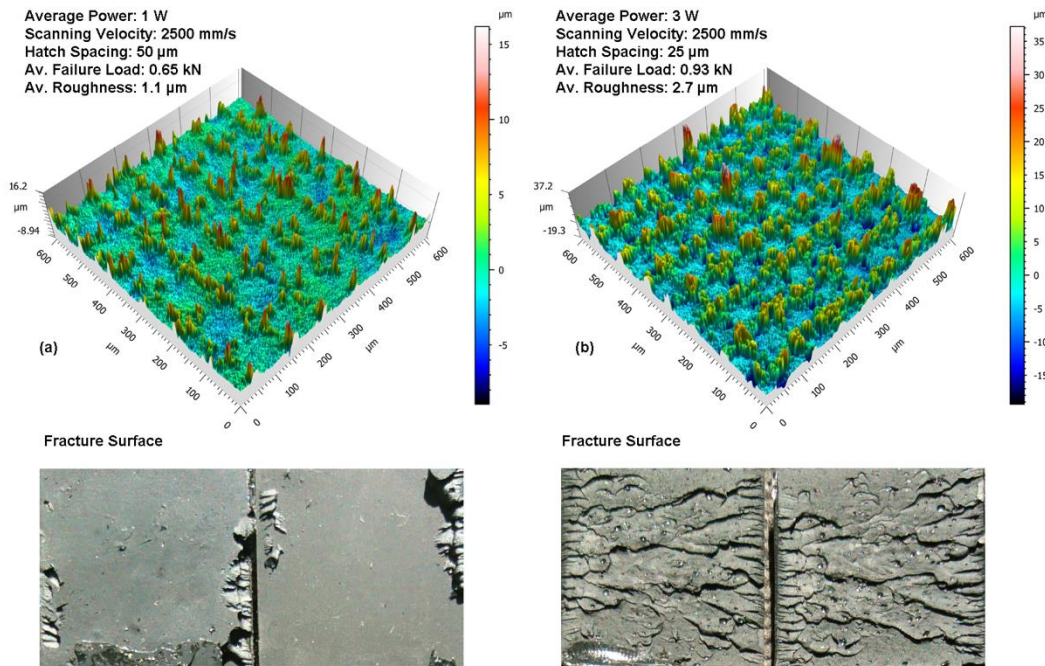

Fig. 12 Measured topography of selected laser-treated surfaces and photographs of corresponding fracture surfaces for group 2, CL scanning strategy. Photographs show both 25 × 25 mm facture surfaces for each individual test specimen.

4 CONCLUSION

Nanosecond pulse laser irradiation with optimized processing parameters has been shown to be an effective method of increasing the strength of adhesive-bonded pigmented PE joints. Though the process was found to be sensitive to heat accumulation at low scanning velocities, a relatively large parameter range was defined over which cohesive failure of Teroson 9399 took place and joints were of consistently high strength. Highest failure load was achieved where the energy dose could be maximized prior to onset of macroscopic melting effects and degradation of the polymer surface, requiring laser scanning strategies that minimized heat accumulation as much as possible. Such effects were less severe in the lateral (hatch) direction and for multiple laser passes, for which the crossed-line strategy with a large pulse separation distance in the scanning direction and lower separation in the lateral direction led to optimum results. Average failure loads of up to 0.93 kN (1.49 MPa, standard deviation 0.01 kN) were achieved with a crossed-line laser scanning strategy and 25 µm hatch spacing, 3 W average power and 2500 mm/s scanning velocity. This outcome represented a 79 % improvement over standard primed joints and an order-of-magnitude improvement over washed joints. These results demonstrate that traditional chemical activation can effectively be replaced by laser treatment, increasing the environmental sustainability of adhesive-bonded joints. Application of standard DoE approaches proved to be effective at optimizing process parameters and could therefore be applied to different polymer-adhesive combinations. Laser treatment of this particular pigmented polymer required low average power, implying that upscaling could be achieved at relatively low cost for high-throughput applications. The process therefore shows promise for industrial implementation, suggesting further investigation should be undertaking into upscaling and new polymer-adhesive combinations.

REFERENCES

[1] Friedrich HE. Challenges of materials technology for low consumption vehicle concepts. Advanced Engineering Materials 2003;5:105-12. https://doi.org/10.1002/adem.200390014

[2] Liu F, Lu X, Zhao L, Zhang J, Xu J, Hu N. Investigation of bolt load redistribution and its effect on failure prediction in double-lap, multi-bolt composite joints. Composite Structures 2018;202:397-405. https://doi.org/10.1016/j.compstruct.2018.02.043

[3] Ebnesajjad S. Surface treatment of materials for adhesive bonding. Oxford: William Andrew; 2014.

[4] ASTM D2093 - 03(2017) Standard practice for preparation of surfaces of plastics prior to adhesive bonding. West Conshohocken: ASTM International; 2017.

[5] Galantucci LM, Gravina A. Surface treatment for adhesive-bonded joints by excimer laser. Composites Part A 1996;27A:1041-9. https://doi.org/10.1016/1359-835X(96)88890-7

[6] Baburaj EG, Starikov D, Evans J, Shafeev GA, Bensaoula A. Enhancement of adhesive joint strength by laser surface modification. International Journal of Adhesion and Adhesives 2007;27:268-76. https://doi.org/10.1016/j.ijadhadh.2006.05.004

[7] Rechner R, Jansen I, Beyer E. Influence of the strength and aging resistance of aluminium joints by laser pre-treatment and surface modification. International Journal of Adhesion and Adhesives 2010;30:595-602. https://doi.org/10.1016/j.ijadhadh.2010.05.009

[8] Loutas TH, Kliafa PM, Sotiriadis G, Kostopoulos V. Investigation of the effect of green laser pre-treatment of aluminum alloys through a design-of-experiments approach. Surface and Coatings Technology 2019;375:370-82. https://doi.org/10.1016/j.surfcoat.2019.07.044

[9] Pan Y, Wu G, Huang Z, Li M, Ji S, Zhang Z. Effects of surface pre-treatments on Mode I and Mode II interlaminar strength of CFRP/Mg laminates. Surface and Coatings Technology 2017;319:309-17. https://doi.org/10.1016/j.surfcoat.2017.04.010

[10] Atanasov PA. Laser welding of plastics: Theory and experiments. Optical Engineering 1995;24. https://doi.org/10.1117/12.210747

[11] Choudhury IA, Shirley S. Laser cutting of polymeric materials: An experimental investigation. Optics & Laser Technology 2010;42:503-8. https://doi.org/10.1016/j.optlastec.2009.09.006

[12] Coelho JMP, Abreu MA, Rodrigues FC. High-speed laser cutting of superposed thermoplastic films: Thermal modeling and process characterization. Optics and Lasers in Engineering 2004;42:27-39. https://doi.org/10.1016/S0143-8166(03)00071-X

[13] Dyer PE, Excimer laser polymer ablation: Twenty years on. Applied Physics A 2003;77:167-73. https://doi.org/10.1007/s00339-003-2137-1

[14] Caiazzo F, Curcio F, Daurelio G, Minutolo FMC. Laser cutting of different polymeric plastics (PE, PP and PC) by a CO_2 laser beam. Journal of Materials Processing Technology 2005;159:279-285. https://doi.org/10.1016/j.jmatprotec.2004.02.019

[15] Eltawahni HA, Olabi AG, Benyounis KY. Effect of process parameters and optimization of CO_2 laser cutting of ultra high-performance polyethylene. Materials & Design 2010;31:4029-38. https://doi.org/10.1016/j.matdes.2010.03.035

[16] Lippert T. Interaction of photons with polymers: From surface modification to ablation. Plasma Processes and Polymers 2005;2:525-46. https://doi.org/10.1002/ppap.200500036

[17] Ilie M, Kneip J-C, Matteï S, Nichici A, Roze C, Girasole T. Through-transmission laser welding of polymers – temperature field modeling and infrared investigation. Infrared Physics & Technology 2007;51:73-9. https://doi.org/10.1016/j.infrared.2007.02.003

[18] Sohn I-B, Noh Y-C, Kim Y-S, Ko D-K, Lee J-M, Choi Y-J. Laser ablation of polypropylene films using nanosecond, picosecond, and femtosecond laser. Journal of the Optical Society of Korea 2008;12:38-41. https://doi.org/10.3807/JOSK.2008.12.1.038

[19] Lawrence J, Li L. Wettability characteristics of polyethylene modified with CO2, Nd:YAG, excimer and high power diode lasers. Proceedings of the Institution of Mechanical Engineers, Part B: Journal of Engineering Manufacture 2001;215:1735-1744. https://doi.org/10.1177/095440540121501207

[20] Riveiro A, Soto R, del Val J, Comesana R, Boutinguiza M, Quintero F, Lusquinos F, Pou J. Laser surface modification of ultra-high-molecular-weight polyethylene (UHMWPE) for biomedical applications. Applied Surface Science 2014;302:236-242. https://doi.org/10.1016/j.apsusc.2014.02.130

[21] Moroni F, Romoli L, Khan MMA. Design of laser-textured surfaces to enhance the strength of adhesively bonded joints. International Journal of Adhesion and Adhesives 2018;85:208-18. https://doi.org/10.1016/j.ijadhadh.2018.06.001

[22] Romoli L, Moroni F, Khan MMA. A study on the influence of surface laser texturing on the adhesive strength of bonded joints in aluminium alloys. CIRP Annals 2017;66:237-240. https://doi.org/10.1016/j.cirp.2017.04.123

[23] Sun C, Min J, Lin J, Wan H, Yang S, Wang S. The effect of laser ablation treatment on the chemistry, morphology and bonding strength of CFRP joints. International Journal of Adhesion and Adhesives 2018;84:325-34. https://doi.org/10.1016/j.ijadhadh.2018.04.014

[24] Technical data sheet. Teroson MS 9399. Düsseldorf: Henkel AG & Co.KGaA; 2014

[25] Montgomery DC, Runger GC. Applied statistics and probability for engineers. New York: John Wiley & Sons; 2011.

[26] Anderson MJ, Whitcomb PJ, RSM Simplified: Optimizing Processes Using Response Surface Methods for Design of Experiments. Productivity Press 2016, ISBN 9781498745987

[27] ISO 25178-2:2012 Geometrical product specifications (GPS) – Surface texture: Areal – Part 2: Terms, definitions and surface texture parameters. Geneva: International Organization for Standardization; 2012.

[28] ASTM D3163 - 01(2014) Standard test method for determining strength of adhesively bonded rigid plastic lap-shear joints in shear by tension loading. West Conshohocken: ASTM International; 2014.

APPENDIX

Table 6 ANOVA table [25] for the first group of experiments with the PL scanning strategy

Source	Sum of Squares	Degrees of Freedom	Mean Square	F Value	p-value Prob > F
Model	4.80×10^{-1}	7	6.80×10^{-2}	8.93	$< 1.00 \times 10^{-4}$
P-Average Power	7.31×10^{-3}	1	7.31×10^{-3}	0.96	3.39×10^{-1}
h-Hatch Spacing	2.67×10^{-4}	1	2.67×10^{-4}	0.04	8.53×10^{-1}
v-Scan. Velocity	7.40×10^{-2}	1	7.40×10^{-2}	9.67	5.30×10^{-3}
Ph	1.20×10^{-2}	1	1.20×10^{-2}	1.63	2.16×10^{-1}
Pv	1.30×10^{-1}	1	1.30×10^{-1}	16.80	5.00×10^{-4}
hv	1.30×10^{-1}	1	1.30×10^{-1}	17.46	4.00×10^{-4}
Phv	1.10×10^{-1}	1	1.10×10^{-1}	14.96	9.00×10^{-4}
Residual	1.60×10^{-1}	21	7.63×10^{-3}		
Lack of Fit	6.88×10^{-3}	1	6.88×10^{-3}	0.9	3.55×10^{-1}
Pure Error	1.50×10^{-1}	20	7.67×10^{-3}		
Cor Total	6.40×10^{-1}	28			

Table 7 ANOVA table for the second group of experiments with the PL scanning strategy

Source	Sum of Squares	Degrees of Freedom	Mean Square	F Value	p-value Prob > F
Model	2.77×10^{-1}	6	4.62×10^{-2}	5.87	6.00×10^{-4}
P-Average Power	5.12×10^{-7}	1	5.12×10^{-7}	0.00	9.94×10^{-1}
h-Hatch Spacing	2.60×10^{-2}	1	2.60×10^{-2}	3.30	8.11×10^{-2}
v-Scan. Velocity	3.44×10^{-3}	1	3.44×10^{-3}	0.44	5.14×10^{-1}
Ph	7.06×10^{-2}	1	7.06×10^{-2}	8.96	6.10×10^{-3}
Pv	1.38×10^{-2}	1	1.38×10^{-2}	1.75	1.98×10^{-1}
hv	5.10×10^{-2}	1	5.10×10^{-2}	6.47	1.75×10^{-2}
Residual	1.97×10^{-1}	25	7.87×10^{-3}		
Lack of Fit	7.58×10^{-2}	8	9.48×10^{-3}	1.33	2.94×10^{-1}
Pure Error	1.21×10^{-1}	17	7.12×10^{-3}		
Cor Total	4.74×10^{-1}	31			

Table 8 ANOVA table for the first group of experiments with the CL scanning strategy

Source	Sum of Squares	Degrees of Freedom	Mean Square	F Value	p-value Prob > F
Model	6.22×10^{-1}	7	8.88×10^{-2}	9.74	$< 1.00\times10^{-4}$
P-Average Power	7.07×10^{-4}	1	7.07×10^{-4}	0.08	7.83×10^{-1}
h-Hatch Spacing	1.20×10^{-3}	1	1.20×10^{-3}	0.13	7.21×10^{-1}
v-Scan. Velocity	6.22×10^{-2}	1	6.22×10^{-2}	6.82	1.63×10^{-2}
Ph	5.49×10^{-2}	1	5.49×10^{-2}	6.03	2.29×10^{-2}
Pv	8.09×10^{-2}	1	8.09×10^{-2}	8.87	7.20×10^{-3}
hv	3.54×10^{-2}	1	3.54×10^{-2}	3.88	6.22×10^{-2}
Phv	6.70×10^{-3}	1	6.70×10^{-3}	0.73	4.01×10^{-1}
Residual	1.91×10^{-1}	21	9.12×10^{-3}		
Lack of Fit	1.45×10^{-1}	1	1.45×10^{-1}	61.6	$< 1.00\times10^{-4}$
Pure Error	4.69×10^{-2}	20	2.35×10^{-3}		
Cor Total	8.13×10^{-1}	28			

Table 9 ANOVA table for the second group of experiments with the CL scanning strategy

Source	Sum of Squares	Degrees of Freedom	Mean Square	F Value	p-value Prob > F
Model	1.04×10^{-1}	6	1.74×10^{-2}	6.24	4.00×10^{-4}
P-Average Power	4.73×10^{-3}	1	4.73×10^{-3}	1.70	2.04×10^{-1}
h-Hatch Spacing	5.26×10^{-3}	1	5.26×10^{-3}	1.89	1.81×10^{-1}
v-Scan. Velocity	1.38×10^{-2}	1	1.38×10^{-2}	4.97	3.49×10^{-2}
Ph	1.34×10^{-2}	1	1.34×10^{-2}	4.81	3.78×10^{-2}
Pv	1.19×10^{-2}	1	1.19×10^{-2}	4.29	4.88×10^{-2}
hv	3.74×10^{-2}	1	3.74×10^{-2}	13.44	1.20×10^{-3}
Residual	6.96×10^{-2}	25	2.78×10^{-3}		
Lack of Fit	1.89×10^{-2}	8	2.36×10^{-3}	0.79	6.18×10^{-1}
Pure Error	5.07×10^{-2}	17	2.98×10^{-3}		
Cor Total	1.74×10^{-1}	31			

Table 10 Averages and standard deviations of failure loads for group 1, PL scanning strategy. Best performing parameters in bold.

Average power [W]	Scanning velocity [mm/s]	Hatch spacing [µm]	Average failure load [kN]	Failure load standard deviation [kN]
1	700	50	0.73	0.15
1	700	150	0.45	0.01
1	2100	50	0.42	0.03
1	2100	150	0.30	0.01
2	1400	100	0.53	0.09
3	700	50	0.44	0.11
3	700	150	0.52	0.07
3	**2100**	**50**	**0.69**	**0.14**
3	2100	150	0.39	0.05

Table 11 Averages and standard deviations of failure loads for group 2, PL scanning strategy. Best performing parameters in bold.

Average power [W]	Scanning velocity [mm/s]	Hatch spacing [µm]	Average failure load [kN]	Failure load standard deviation [kN]
2	**1700**	**25**	**0.85**	**0.03**
2	1700	50	0.66	0.10
2	2100	37.5	0.75	0.07
2	2500	25	0.77	0.04
2	2500	50	0.38	0.02
3	1700	37.5	0.73	0.01
3	2100	25	0.70	0.02
3	2100	37.5	0.66	0.06
3	2100	50	0.60	0.09
3	2500	37.5	0.80	0.09
4	1700	25	0.67	0.02
4	1700	50	0.76	0.04
4	2100	37.5	0.67	0.04
4	2500	25	0.73	0.07
4	2500	50	0.58	0.10

Table 12 Averages and standard deviations of failure loads for group 1, CL scanning strategy. Best performing parameters in bold.

Average power [W]	Scanning velocity [mm/s]	Hatch spacing [µm]	Average failure load [kN]	Failure load standard deviation [kN]
1	700	50	0.78	0.02
1	700	150	0.55	0.07
1	2100	50	0.74	0.02
1	2100	150	0.30	0.02
2	1400	100	0.77	0.04
3	700	50	0.52	0.06
3	700	150	0.55	0.10
3	**2100**	**50**	**0.79**	**0.03**
3	2100	150	0.46	0.02

Table 13 Averages and standard deviations of failure loads for group 2, CL scanning strategy. Best performing parameters in bold.

Average power [W]	Scanning velocity [mm/s]	Hatch spacing [µm]	Average failure load [kN]	Failure load standard deviation [kN]
1	1700	25	0.82	0.08
1	1700	50	0.78	0.03
1	2100	37.5	0.78	0.07
1	2500	25	0.91	0.05
1	2500	50	0.65	0.03
2	1700	37.5	0.85	0.01
2	2100	25	0.83	0.06
2	2100	37.5	0.85	0.02
2	2100	50	0.80	0.12
2	2500	37.5	0.81	0.01
3	1700	25	0.75	0.10
3	1700	50	0.80	0.02
3	2100	37.5	0.80	0.05

3	2500	25	0.93	0.01
3	2500	50	0.81	0.05